CHEMISTRY OF MATERIALS
Article
pubs.acs.org/cm

Second Harmonic Generation Response Optimized at Various Optical Wavelength Ranges through a Series of Cubic Chalcogenides Ba$_6$Ag$_{2.67+4\delta}$Sn$_{4.33-\delta}$S$_{16-x}$Se$_x$

Wei-Han Lai,[†] Alyssa S. Haynes,[‡] Laszlo Frazer,[§] Yu-Ming Chang,[∥] Te-Kun Liu,[†] Jyun-Fan Lin,[†] I-Chu Liang,[†] Hwo-Shuenn Sheu,[⊥] John B. Ketterson,[§] Mercouri G. Kanatzidis,[‡] and Kuei-Fang Hsu*[,†]

[†]Department of Chemistry and Center for Micro/Nano Science and Technology, National Cheng Kung University, Tainan 701, Taiwan

[‡]Department of Chemistry, Northwestern University, Evanston, Illinois 60208, United States

[§]Department of Physics and Astronomy, Northwestern University, Evanston, Illinois 60208, United States

[∥]Center for Condensed Matter Sciences, National Taiwan University, Taipei 106, Taiwan

[⊥]National Synchrotron Radiation Research Center, Hsinchu 300, Taiwan

Supporting Information

ABSTRACT: A new series of metal chalcogenides with the formula Ba$_6$Ag$_{2.67+4\delta}$Sn$_{4.33-\delta}$S$_{16-x}$Se$_x$ (x = 0 for **1**, x = 6.47 for **2**, and x = 16 for **3**) were synthesized. Compounds **1**−**3** are isotypic with a three-dimensional structure and crystallize in the noncentrosymmetric space group $I\bar{4}3d$. The framework in **1** is constructed by alternative corner-sharing of AgS$_4$ and SnS$_4$ tetrahedra with Ba^{2+} cations distributed within the channels. The Ag$^+$ atoms are disordered with two neighboring silver sites trapped in various coordination environments. Selected area electron diffraction (SAED) patterns from samples of **1** indicate that the structural lattice is ordered without evidence of long-range ordering. High resolution electron microscopy (HREM) images of **1** along the [001] direction display the body-centered arrangement of barium atoms and the periodic appearance of lines between barium atoms that correspond to part of the array of disordered silver atoms. Within the sulfide composition range, the solid solutions are Ba$_6$Ag$_{2.67+4\delta}$Sn$_{4.33-\delta}$S$_{16}$ with δ = 0.13 for **1**, 0.31 for **1a**, and 0.33 for **1b**; the crystal colors range from dark-red to orange and yellow, respectively. All compounds are transparent in the mid-infrared region and have absorption edges ranging from 1.27 to 2.37 eV. The significant second harmonic generation (SHG) intensities of the five materials are optimized at wavelengths ranging from 600 to 800 nm. The outstanding ones are **1a** and **2** which display strong intensities 4.4−11.6 times and 2.2−10.4 times that of AgGaSe$_2$ in the ranges 600−700 nm and 675−800 nm, respectively. Raman spectroscopic characterization is reported.

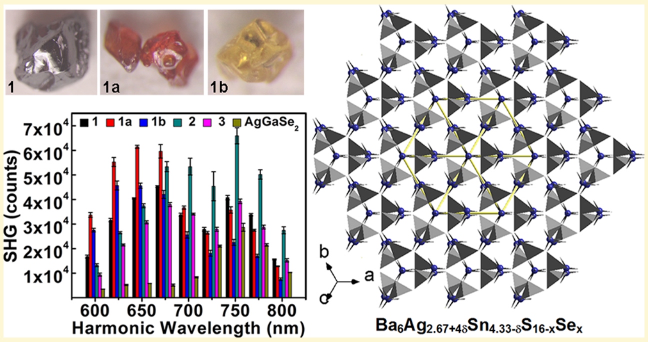

■ INTRODUCTION

Generation of coherent mid-infrared radiation is important in diverse applications in molecular spectroscopy,[1−4] telecommunications,[5−8] sensing of atmospheric gases,[9,10] and optical biomarkers.[11−14] Highly efficient generation of mid-infrared radiation occurs through the nonlinear optical (NLO) second harmonic generation process, and in the 2−12 μm range it is performed using the commercial chalcopyrite semiconductors AgGaQ$_2$ (Q = S, Se) which exhibit wide infrared transparency, high nonlinearity, and moderate birefringence but poor laser damage thresholds.[15−21] The phases of AgGaGeS$_4$[22] and AgGaGe$_5$Se$_{12}$[23] created by the addition of GeQ$_2$ to AgGaQ$_2$ as well as the lithium-based derivatives LiInSe$_2$,[24] LiGaS$_2$,[25] Li$_2$GeGa$_2$S$_6$,[26] and Li$_2$CdGeS$_4$[27] have their absorption edges shifted to higher energy, but the nonlinear coefficients are seriously decreased. The development of new materials using solid state chemistry that combine strong NLO SHG response and wide band gap is an ongoing active area of research.[28]

Recently, many multinary chalcogenides composed of distinct MQ$_4$ tetrahedra with M = Cu$^+$, Ag$^+$, Cd^{2+}, Hg^{2+}, Ga^{3+}, In^{3+}, Ge^{4+}, and Sn^{4+} metals have been reported to be potential infrared NLO candidates. Examples include BaGa$_4$Q$_7$,[29,30] Ln$_4$SbGaS$_9$ (Ln = lanthanide cations),[31] Ba$_4$AgM$_5$Se$_{12}$ (M = Ga, In),[32] ACd$_4$Ga$_5$Q$_{12}$ (A = K, Rb, Cs),[33] Ba$_{23}$Sb$_2$Ga$_8$S$_{38}$,[34] Ba$_3$AGa$_5$Se$_{10}$Cl$_2$ (A = K, Rb, Cs),[35] Ba$_4$CuGa$_5$Q$_{12}$,[36] Dy$_3$GaS$_6$,[37] K$_2$Hg$_3$M$_2$S$_8$ (M = Ge, Sn),[38] Na$_2$Ge$_2$Se$_5$,[39] BaGa$_2$GeQ$_6$,[40] Li$_2$In$_2$MQ$_6$ (M = Si, Ge),[41] Ba$_7$Sn$_5$S$_{15}$,[42] and La$_2$Ga$_2$GeS$_8$.[43] The chalcophosphate-based

Received: November 26, 2014
Revised: January 29, 2015
Published: January 30, 2015

Table 1. Crystal Data and Refinement Details for Compounds 1−3

	compound				
	1	**1a**	**1b**	**2**	**3**
formula	$Ba_6Ag_{3.21(4)}Sn_{4.20}S_{16}$	$Ba_6Ag_{3.92(4)}Sn_{4.02}S_{16}$	$Ba_6Ag_{4.00(6)}Sn_{4.00}S_{16}$	$Ba_6Ag_{3.57(6)}Sn_{4.11}S_{9.53}Se_{6.47(2)}$	$Ba_6Ag_{3.63(8)}Sn_{4.09}Se_{16}$
formula weight	2181.84	2237.06	2243.31	2513.40	2964.41
crystal system	cubic	cubic	cubic	cubic	cubic
space group	$I\bar{4}3d$	$I\bar{4}3d$	$I\bar{4}3d$	$I\bar{4}3d$	$I\bar{4}3d$
a (Å)	14.7432(2)	14.7422(7)	14.7482(3)	14.9596(2)	15.2983(3)
V (Å^3)	3204.6(1)	3204.0(3)	3207.9(1)	3347.8(1)	3580.4(1)
Z	4	4	4	4	4
ρ_{calcd} (g cm^{-3})	4.510	4.639	4.645	4.986	5.499
μ (mm^{-1})	13.345	13.690	13.703	19.607	27.464
$F(000)$	3803	3911	3920	4327	5020
T (K)	293	293	293	293	293
total refls.	11660	11540	9759	12019	12943
unique refls.	673	672	672	691	747
(R_{int})	(0.0429)	(0.0263)	(0.0282)	(0.0291)	(0.0511)
goodness-of-fit	1.133	1.110	1.115	1.105	1.043
$R_1{}^a$ $[I > 2\sigma(I)]$	0.0185	0.0215	0.0239	0.0202	0.0266
$wR_2{}^b$ $[I > 2\sigma(I)]$	0.0411	0.0571	0.0642	0.0520	0.0664
largest diff. peak and hole (e Å^{-3})	0.808 and −1.277	1.049 and −1.300	1.548 and −2.272	1.127 and −1.525	1.182 and −1.604

[a] $R_1 = (\sum||F_o| - |F_c||)/\sum|F_o|$. [b] $wR_2 = \{\sum[w(F_o{}^2 - F_c{}^2)^2]/\sum[w(F_o{}^2)^2]\}^{1/2}$.

Table 2. Atomic Coordinates, Thermal Parameters (Å^2), and Occupancies for 1−3

atom	x/a	y/b	z/c	$U_{eq}{}^a$	sof
1					
Ba(1)	0.76769(3)	1/2	1/4	0.0241(2)	1
Sn(1)	0.97923(2)	0.52077(2)	0.47923(2)	0.0149(2)	1
Ag(1)	3/4	3/8	1/2	0.0359(5)	0.857(5)
Ag(1A)	3/4	0.3097(13)	1/2	0.0359(9)	0.071(2)
Ag(1B)	3/4	0.2455(10)	1/2	0.0359(9)	0.069(2)
S(1)	0.88687(9)	0.61313(9)	0.38687(9)	0.0242(5)	1
S(2)	0.89103(8)	0.43441(8)	0.58576(8)	0.0169(2)	1
2					
Ba(1)	0	3/4	0.48043(4)	0.0287(2)	1
Sn(1)	0.02038(2)	0.47962(2)	0.52038(2)	0.0156(2)	1
Ag(1)	1/4	5/8	1/2	0.0475(7)	0.780(6)
Ag(1A)	1/4	0.6885(12)	1/2	0.0475(11)	0.111(3)
Ag(1B)	1/4	0.7589(9)	1/2	0.0475(11)	0.112(4)
S/Se(1)	0.11259(9)	0.38741(9)	0.61259(9)	0.0295(8)	0.859/0.141(12)
S/Se(2)	0.11019(6)	0.56682(6)	0.41226(6)	0.0198(3)	0.508/0.492(7)
3					
Ba(1)	0	3/4	0.48286(6)	0.0263(2)	1
Sn(1)	0.01834(4)	0.48166(4)	0.51834(4)	0.0142(2)	1
Ag(1)	1/4	5/8	1/2	0.0518(13)	0.762(9)
Ag(1A)	1/4	0.6900(20)	1/2	0.0518(15)	0.107(4)
Ag(1B)	1/4	0.7581(12)	1/2	0.0518(15)	0.133(5)
Se(1)	0.11233(6)	0.38767(6)	0.61233(6)	0.0340(4)	1
Se(2)	0.10905(6)	0.56954(5)	0.41170(5)	0.0175(2)	1

[a] U_{eq} is defined as one-third of the trace of the orthogonalized U_{ij} tensor.

$K_2P_2Se_6$,[44] $Cs_5BiP_4Se_{12}$,[45] $APSe_6$ (A = K, Rb),[46] and $A_4GeP_4Q_{12}$ (A = K, Rb, Cs)[47] represent another family that have PQ_4 tetrahedra aggregated as polar chains. Several of the materials exhibit strong SHG intensities and intrinsic phase matching at characterized wavelengths.[27,29,39,40,42,44,46]

We have previously reported a series of potential infrared NLO materials of $Ba_4CuGa_5Q_{12}$ (Q = S, $S_{0.75}Se_{0.25}$, Se)[36] belonging to the tetragonal $\bar{4}2m$ crystal system as that of chalcopyrite semiconductors. Here we introduce the new series $Ba_6Ag_{2.67+4\delta}Sn_{4.33-\delta}Q_{16}$ (Q = S, $S_{0.59}Se_{0.41}$, Se; $0.13 \leq \delta \leq 0.33$) belonging to the cubic $\bar{4}3m$ crystal system as new NLO materials with strong SHG response. Solid solutions in this group generate compounds with systematically varying band gaps and display strong SHG intensities at specific optical ranges that are superior to those of the benchmark $AgGaSe_2$.

■ EXPERIMENTAL SECTION

Synthesis and Characterization. The chemicals used in the reactions were barium (rod, 99.99%, Aldrich), silver (shot, 99.9%), tin (pieces, 99.9%, Aldrich), sulfur (powder, 99.98%, Aldrich), selenium (pellet, 99.98%, Aldrich), and potassium bromide (crystals, 99.9%, J. T. Baker). All manipulations were conducted under a dry N_2 atmosphere in an OMNI-LAB glovebox. The chemicals were loaded in fused silica tubes (diameter: 8 mm) and sealed under vacuum (<10^{-4} Torr).

Syntheses of $Ba_6Ag_{3.21(4)}Sn_{4.20}S_{16}$ *(1),* $Ba_6Ag_{3.92(4)}Sn_{4.02}S_{16}$ *(1a), and* $Ba_6Ag_{4.00(6)}Sn_{4.00}S_{16}$ *(1b).* A mixture of 6.00 mmol of Ba, 3.21 mmol of Ag, 4.20 mmol of Sn, 16.00 mmol of S, and 4.20 mmol of KBr was heated at 300 °C for 4 h, raised to 800 °C and kept there for 48 h, cooled to 300 °C within 100 h, and finished by turning off the power. Dark-red irregular-shape crystals of **1** were obtained in the final product. Deionized water was used to remove the KBr flux in an ultrasonic cleaner. On the basis of the stoichiometric composition of $Ba_6Ag_{2.67+4\delta}Sn_{4.33-\delta}S_{16}$, slight adjustment of the Ag/Sn molar ratio produced crystals appearing with various colors. Dark-red crystals of **1** were obtained as a single product with the range of $0.0 < \delta < 0.24$. The yield of **1** was about 72% prepared at $\delta = 0.13$ (mainly because of sample loss sticking on the walls of the silica tubes). Orange crystals of **1a** grew gradually with **1** in the product with increasing values of δ. The major product of **1a** was obtained using the range of $0.30 < \delta < 0.40$ in the reactions. The yield of **1a** was about 70% prepared at $\delta = 0.31$. However, several large crystals of **1** coexisted with **1a** in the final product. The materials can be separated with forceps under an optical microscope. The continued increase of δ values caused yellow crystals of **1b** to precipitate with **1**, **1a**, or both in the final products. The large amount of **1b** prepared at $\delta = 0.58$ was about half of the 70% crystal yield. The other half of the product was large crystals of **1**. Crystals of **1**, **1a**, and **1b** were stable in air and water.

Syntheses of $Ba_6Ag_{3.57(6)}Sn_{4.11}S_{9.53}Se_{6.47(2)}$ *(2) and* $Ba_6Ag_{3.63(8)}Sn_{4.09}Se_{16}$ *(3).* A mixture of 6.00 mmol of Ba, 3.57 mmol of Ag, 4.11 mmol of Sn, 9.53 mmol of S, 6.47 mmol of Se, and 4.20 mmol of KBr was reacted in the same heating profile as that operated for **1**. Dark-red crystals of **2** with a yield of about 50% were observed as a single product. A mixture of 6.00 mmol of Ba, 3.63 mmol of Ag, 4.09 mmol of Sn, 16.00 mmol of S, and 4.20 of mmol KBr was reacted in the same heating profile. Dark-red crystals of **3** with a yield of about 66% were obtained as a single product. Dimethylformamide (DMF) was used to remove the KBr flux since crystals of **2** and **3** dissolved completely in water giving black solutions. The loss of sample stuck on the wall of the silica tubes and the slight solubility of **2** and **3** in DMF lead to lower yields of both compounds as compared with **1**. The surfaces of crystals of **2** and **3** were ashed in a few days when exposed to ambient moisture.

Physical Measurements. *Single-Crystal X-ray Diffraction Analysis.* Single crystals were selected for indexing and data collection on a Bruker APEXII CCD diffractometer, irradiating with graphite-monochromatized Mo Kα radiation (λ = 0.71073 Å). Data integrations and empirical absorption corrections were performed using the *SAINT* and *SADABS* functions, respectively, in the *APEX*2 package.[48] The structures were solved and refined using the *SHELXTL*-97 package.[49]

For compound **1**, the space group was determined to be $I\bar{4}3d$, based on intensity distributions and systematic absences of the observed structure factors (Table 1). Direct methods were used to locate Ba(1), Sn(1), Ag(1), S(1), and S(2) atoms on the electron density maps (Table 2). All the atoms were fully occupied on the crystallographic sites except for the Ag(1) atom refined with an occupancy of 85.7(5)% on a $\bar{4}$ axis. The Ag(1A) and Ag(1B) atoms were located around the Ag(1) site and fell on a 2-fold axis with low occupancies of 7.1(2)% and 6.9(2)%, respectively. The occupancies of Ag(1), Ag(1A), and Ag(1B) sites were refined without restrictions, but thermal parameters were constrained at the same value. In the end of the structural description section we discuss in detail the disordering behavior. A small amount of Sn atoms were required to be present within these silver sites to obtain a charge-balanced formula for **1**. The calculation of bond-valence sums gave the charges of 1.13, 1.01, and 0.64 for the Ag(1), Ag(1A), and Ag(1B) sites, respectively.[50] An ideal parent formula was first calculated to be $Ba_6Ag_{2.67}Sn_{4.33}S_{16}$ as the Ag(1) site was assumed to be fully occupied at the $\bar{4}$ position. The refinements of partial Sn occupancies on these severely disordered Ag sites do not converge. Therefore, the charge-balanced formula of **1** was determined to be $Ba_6Ag_{2.67+4\delta}Sn_{4.33-\delta}S_{16}$ with $\delta = 0.13$ based on an estimated 5.89% of Sn distributed among the three Ag sites. All the atoms in **1** were refined anisotropically with R_1 and wR_2 converged at 0.0185 and 0.0411, respectively. Crystals **1a** and **1b** adopt the same structure as that determined in **1**. The charge-balanced formulas of **1a** and **1b** were determined to be $Ba_6Ag_{2.67+4\delta}Sn_{4.33-\delta}S_{16}$ with $\delta = 0.31$ and 0.33, respectively. All the atoms in **1a** and **1b** were refined anisotropically. The values of R_1 and wR_2 converged at 0.0215 and 0.0571 for **1a** and 0.0239 and 0.0642 for **1b**, respectively.

In the structure of **2**, the refinements of S(1)/Se(1′) and S(2)/Se(2′) distributions gave percentages of 0.859/0.141(12) and 0.508/0.492(7), respectively. The resulting formula of **2** was $Ba_6Ag_{2.67+4\delta}Sn_{4.33-\delta}S_{9.53}Se_{6.47}$ with $\delta = 0.22$. All atoms were refined anisotropically with R_1 and wR_2 converged at 0.0202 and 0.0520, respectively. The formula of **3** is $Ba_6Ag_{2.67+4\delta}Sn_{4.33-\delta}Se_{16}$ with $\delta = 0.24$. All atoms were refined anisotropically with R_1 and wR_2 converged at 0.0266 and 0.0664, respectively.

Powder X-ray Diffraction. The measured powder pattern of **1** was collected at the BL01C2 beamline of the National Synchrotron Radiation Research Center, Taiwan (Supporting Information Figure S1). The powder sample was sealed in a 0.3 mm capillary tube for a transmission type measurement using 18 KeV (0.6888 Å) X-rays. A Mar345 imaging plate detector located at ∼30 cm from the sample position was used to record powder diffraction patterns. 1D powder diffraction patterns were converted from 2D powder rings by using the *Fit2D* program. The X-ray powder patterns of **1a**, **1b**, **2**, and **3** were collected using a Shimadzu XRD-7000s X-ray diffractometer and compared well with the patterns simulated from the results of single-crystal X-ray structural analyses (Supporting Information Figure S2).

Electron Microscopy. Semiquantitative analyses of crystals were performed using a Hitachi SU-1500 scanning electron microscope equipped with a Horiba EMAX-ENERGY energy dispersive spectrometer (EDS). The data were acquired using an accelerating voltage of 10 kV. Crystals of **1**, **1a**, and **1b** prepared by the stoichiometric composition $Ba_6Ag_{2.67+4\delta}Sn_{4.33-\delta}S_{16}$ with different values of δ were selected for the EDS analysis. Dark-red crystals of **1** prepared at δ = 0, 0.18, and 0.24 were characterized as $Ba_{6.0(2)}Ag_{3.9(2)}Sn_{4.2(2)}S_{16.4(4)}$, $Ba_{6.0(2)}Ag_{3.9(2)}Sn_{4.3(2)}S_{16.3(4)}$, and $Ba_{6.0(2)}Ag_{4.1(2)}Sn_{4.4(2)}S_{17.1(5)}$, respectively. Orange crystals of **1a** prepared at δ = 0.3, 0.36, and 0.40 were characterized as $Ba_{6.0(2)}Ag_{4.3(2)}Sn_{4.2(2)}S_{16.5(4)}$, $Ba_{6.0(2)}Ag_{4.5(2)}Sn_{4.3(2)}S_{16.8(5)}$, and $Ba_{6.0(2)}Ag_{4.5(2)}Sn_{4.2(2)}S_{16.7(4)}$, respectively. Yellow crystals of **1b** prepared at δ = 0.58 and 0.64 were characterized as $Ba_{6.0(2)}Ag_{4.5(2)}Sn_{4.2(2)}S_{17.1(6)}$ and $Ba_{6.0(2)}Ag_{4.6(2)}Sn_{4.2(2)}S_{16.8(5)}$, respectively. Dark-red crystals of **2** and **3** were characterized with the average compositions of $Ba_{6.0(4)}Ag_{3.2(5)}Sn_{4.5(5)}S_{9.7(9)}Se_{6.9\ (6)}$ and $Ba_{6.0(4)}Ag_{3.9(4)}Sn_{4.3(4)}Se_{16.8(6)}$, respectively.

The specimens prepared for transmission electron microscopy (TEM) were sliced from the cross section of crystal **1** by dual-beam focused ion beam (DB-FIB) using a FEI Nova-200 NanoLab Compatible system with a field emission electron column at 5 kV and a Ga-based ion column at 30 kV. High-resolution electron microscopy (HREM) images and selected area electron diffraction (SAED) patterns were obtained at 200 kV using a JEM-2100F electron microscope. The noise on the HREM image was filtered after Fourier transformation.

Differential Thermal Analysis. Differential thermal analysis (DTA) was performed using a computer-controlled Shimadzu DTA-50 thermal analyzer. The powder sample and a reference Al_2O_3 were loaded with the same weight, about 25 mg, and sealed in fused silica ampules under vacuum. The DTA chamber was heated to 900 °C at 20 °C min^{-1} and cooled to 100 °C at the same rate. The thermal behavior of samples **1**−**3** was monitored by multiple heating and cooling cycles (Supporting Information Figure S3). The DTA curves displayed that **1** and **2** did not melt in the measured temperature range. The recrystallization of **3** occurred at about 730 °C, but the melting point did not appear obviously to show which temperature may be close to the limit of detection. The powder X-ray diffraction patterns of sample **3** after the measurement of DTA analysis remained in the same phase.

Optical Spectroscopy. Diffuse reflectance spectra were record using a Hitachi U-4100 UV−vis−NIR spectrophotometer covering a wavelength range from 300 to 3300 nm. A single monochromator, photomultiplier detector for the UV/vis region, and PbS-based detector for the NIR region were equipped with the system. The powder sample was measured with respect to $BaSO_4$ powder as a reference. The absorption data (α/S) were calculated from the reflectance data using the Kubelka−Munk function: $\alpha/S = (1 - R)^2/2R$ where R is the reflectance at a given energy, α is the absorption, and S is the scattering coefficient. The scattering coefficient has been shown to be practically wavelength independent for particles larger than 5 μm, which is smaller than the particle size of samples used here. The band gap was determined as the intersection point between the energy axis and the line extrapolated from the linear portion of the absorption edge.[51−53]

The Raman spectra were recorded using a Renishaw inVia Raman microscope with a 785 nm diode laser at 36 mW switched by semiautomatic changing of optical components on a standard baseplate. The exposure time on the surface of the crystal was 10 s. The data collection by Renishaw's RenCam CCD detector was 1 min. High spatial resolution with a minimum laser spot size of ≤1 μm and a spectrum resolution with an 1800 gr/mm grating were applied.

The mid-infrared transmittance spectra were recorded using a PerkinElmer Rx1 FTIR spectrophotometer. The pressed pellets were prepared by grinding the powder samples with KBr and then drying at 70 °C for 1 day. The infrared spectroscopic measurements covered a wavelength range from 400 to 4000 cm^{-1} for the five compounds.

Second-Harmonic Generation Measurements. The setup details for NLO measurements are described, including the laser, the selection of incident laser wavelengths, the use of laser power, the size of the laser spot, the record of SHG signals, and the particle sizes of samples. The fundamental of an Nd:YAG laser pulsed at 10 Hz with a $(5.4 \pm 0.5) \times 10^{-11}$ s full width half-maximum pulse duration was frequency-tripled (355 nm) and used to pump a homemade optical parametric amplifier (OPA). A long wavelength pass filter was used to remove the signal beam, and the idler beam was focused onto the samples with a 5 mm focal length N-BK7 lens with a spot size of order 1 mm. In order to check the SHG efficiency as a function of the excitation energy, we tuned the wavelengths of the incident light from 1200 to 1600 nm. In this range, the spectral bandwidth of the linearly polarized light from the OPA is rather broad, about 2 meV full width at half-maximum. The SHG signal was collected off axis and focused onto a fiber optic bundle. The output of the fiber optic bundle was coupled to the entrance slit of a Spex 500 M spectrometer and detected using a Spectrum One nitrogen-cooled CCD 1000 camera. The data collection time was 20 s.

All samples were crushed into powder and sieved to separate the crystallites into 8 different particle size ranges (20−32 μm, 32−45 μm, 45−53 μm, 53−63 μm, 63−90 μm, 90−106 μm, 106−125 μm, 125−150 μm). Material from each size range was placed into borosilicate capillary tubes (1.5−1.8 mm × 90 mm). The filled capillaries were evacuated and then set into a dry nitrogen environment, capped with clay to retain the dry nitrogen atmosphere, and finally flame-sealed to prevent sample oxidation or hydrolysis.

Reflected Second Harmonic Generation (SHG) Measurement. The experiment was conducted with an 800 nm, 82 MHz, 15 fs Ti-sapphire oscillator (Femto Lasers, model: Femtosource Compact Pro). The femtosecond laser was intensity-modulated by a mechanical chopper and focused on the pellet samples with a 20X, NA0.75 objective (Nikon, model: S Flour 20X). The incident laser power was set to ∼75 mW, and the laser beam spot size was estimated to be ∼1 μm on the sample. The reflected SHG at 400 nm was then collected by the same objective and measured by a 400 nm bandpass-filtered photomultiplier (Hamamatsu PMT, Model: R585) and phase-sensitive lock-in amplifier (Stanford Research System, Model: SR830). In order to verify the power law relation between the laser intensity (I) and reflected SH signal, i.e., SHG $\sim I^2$, the laser power was regulated by rotating an 800 nm half-wave plate located between the laser output and a Glan-Taylor polarizer. The laser intensity can be varied as a function of the half-wave plate angle (θ) and expressed as $I = I_0 \sin^2(2\theta)$, where $I_0 \sim 0.95 \times 10^6$ W/cm^2. The samples of **1** and **3** were prepared as round pellets with polished surfaces. Because of the micrometer size of single crystal grains, it was expected that the femtosecond laser can only focus on a particular facet of the single crystal grain to generate the reflected SH signal in our SHG experiment. By taking the polycrystalline nature of our pellet samples into consideration, we choose six sample spots to perform the laser power dependent SHG measurement to realize the possible orientation of single crystal grains. Meanwhile, we used an n-type GaAs (001) crystal as a reference sample to compare and estimate the SHG conversion efficiency of these studied samples under the identical experimental conditions.

■ RESULTS AND DISCUSSION

Structure Description. All compounds are isostructural with a noncentrosymmetric three-dimensional cubic structure composed of alternative corner-sharing of $Ag(1)Q_4$ and $Sn(1)Q_4$ tetrahedra with Ba^{2+} cations distributed within the channels. The structures crystallize in the same space group as that of $Ba_6Cd_2Sn_4S_{16}$[54] and $Ba_6CdAg_2Sn_4S_{16}$,[54] in which the Wyckoff positions (12b) corresponding to the Ag(1) site in **1** are occupied by 66.7% Cd^{2+} ions and 100% mixture of Cd^{2+}/Ag^+ ions, respectively. Within the framework, the $Sn(1)S_4$ tetrahedra lying on 3-fold axes are arranged by the *d*-glide translation on the {110} planes (Figure 1a). The $Ag(1)S_4$ tetrahedra are further inserted between the layers of $Sn(1)S_4$ tetrahedra and are related by 2-fold and $\bar{4}$ symmetries. The Ba^{2+} ions within the structure are encapsulated within the tunnels along the [111] direction and are coordinated with eight sulfur atoms having the Ba−S distances ranged from 3.153(1) to 3.503(1) Å (Figure 1b and Supporting Information Figure S4 and Table 3).

The Ag(1) site in **1** is deficient with 85.7(5)% on a $\bar{4}$ axis and is disordered with the Ag(1A) and Ag(1B) sites on a 2-fold axis with 7.1(2)% and 6.9(2)% occupancies, respectively (Figure 2). It is well-known that Ag^+ and Cu^+ ions in solid chalcogenides can have low energy barriers and be mobile in the structure.[55] For example, silver ions in $Ln_3Ag_{1-\delta}MS_7$ (M = Ge, Sn) are mobile between trigonal and trigonal-antiprismatic holes along the 6_3 axis and have a Ag···Ag distance of 1.02 Å.[56] In **1**, the Ag(1A)···Ag(1) distance is 0.96(2) Å and additionally appears on the either side of the Ag(1) center since the crystallographic multiplicities are reduced from the $\bar{4}$ to 2-fold. The Ag(1A)−S bonds with two short distances of 2.435(1) Å and two long distances of 3.050(11) Å and the S(2B)−Ag(1A)−S(2C) angle of 175.9(9)° describe the linear or seesaw-like coordination environment. The disordered Ag(1B) site, which is 1.91(1) Å from the Ag(1) site, is trapped in a distorted tetrahedral hole of sulfur atoms with Ag(1B)−S distances of 2.644(6) Å and 3.069(8) Å. Of course, these disordered silver sites having short Ag···Ag distances of less than ∼2 Å are not occupied simultaneously. A possible factor to cause such severe disordered behavior in **1** may be the estimated 5.89% of Sn^{4+} ions present among the Ag^+ sites. Interestingly, the high average cubic symmetry in **1** is unaffected as indicated by the absence of longer range order evident in selected area electron diffraction.

Electron diffraction. Selected area electron diffraction (SAED) was performed on a specimen sliced from crystal **1** in order to examine the possibility of a superstructure that can order these silver positions. The diffraction pattern along the [001] direction displays an ordered cubic body-centered lattice without the observation of extra or diffuse spots (Figure 3a). The ratio of reciprocal spacing $d^*(200)/d^*(110) = 1.422$ is

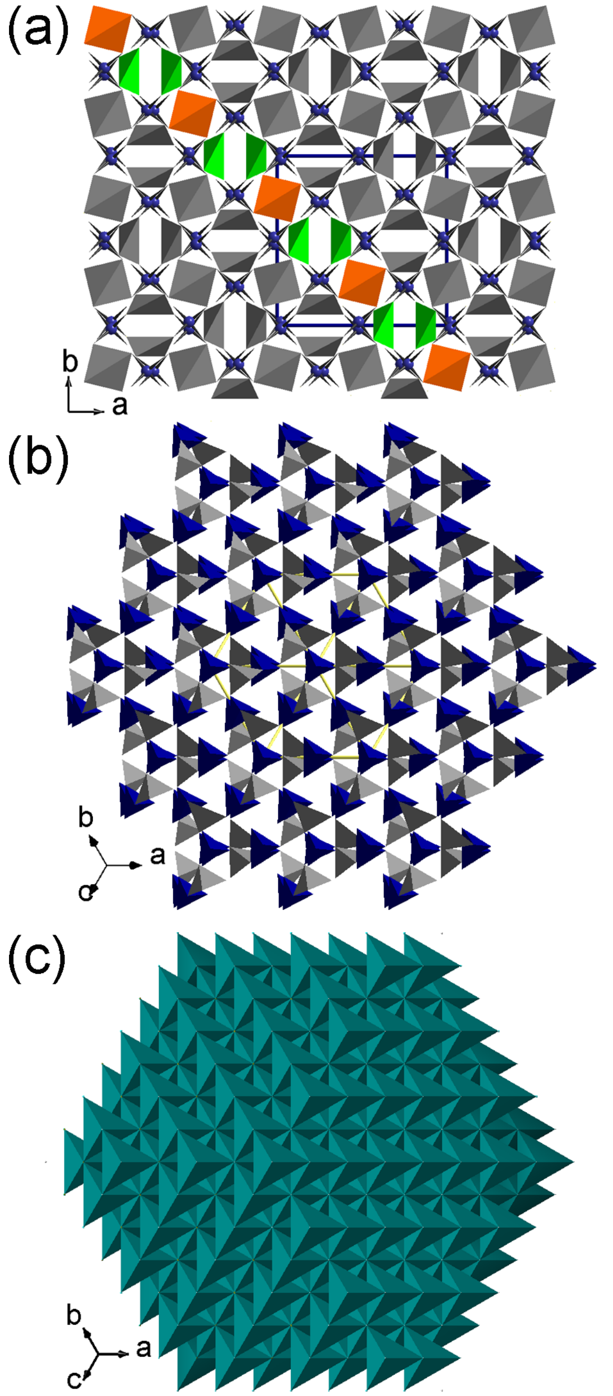

Figure 1. (a) Three-dimensional framework of **1** along the [100] direction. Color scheme: SnS_4 tetrahedra, blue ball and black stick; AgS_4 tetrahedra, gray. The AgS_4 tetrahedra depicted with green color are related by a 2-fold symmetry. The AgS_4 tetrahedra with green and orange colors are related by a $\bar{4}$ rotational operation. (b) A perspective view of the framework along the [111] direction. Color scheme: SnS_4 tetrahedra, blue; AgS_4 tetrahedra, gray. The Ba atoms were omitted for clarity. (c) A perspective view of indigo $GaAs_4$ tetrahedra along the [111] direction

close to the ideal value of 1.414 where the $d(200)$ distance of 7.4 Å is about a half of the cubic lattice dimension.[57] The lattice can be verified again from another [$\bar{1}$13] direction with the ratio of $d^*(121)/d^*(110)$ near an ideal value of 1.732 (Supporting Information Figure S5). A high-resolution electron microscopy (HREM) image along the [001] direction of **1** displays two important structural characteristics (Figure 3b). The inset (i) displays five symmetric spots with intense contrast in the image that correspond to the body-centered arrangement of barium atoms in the unit cell (Figure 3c,d). Figure 3e shows the periodic appearance of lines with less contrast observed between barium atoms at some areas in the image. The orientations and positions of these lines like in the inset (ii) seem to correspond to the disordered silver atoms arranged by the same period along the *a* axis. However, most of the silver atoms arranged between barium atoms are not discernible in the image (Figure 3c).

Solid Solutions. In addition to the end-member with $x = 0$ for **1**, we could also prepare the compositions of $Ba_6Ag_{2.67}Sn_{4.33}S_{16-x}Se_x$ with $x = 6.5$ for **2** and $x = 16$ for **3**. The larger ionic radius of Se relative to S leads to larger unit cell constants which increase linearly with x following Végard's law[58] (Figure 4a). In **2**, the substitution of selenium atoms at 14.1(12)% and 49.2(7)% occurs both at the 3-fold special positions and general positions of the sulfur sites in **1**, respectively. The M−Q (M = Ag, Sn) average bond distances gradually increase in going from **1** to **3**. The reduced electronegativity of Se causes the band gap to decrease from 1.59 to 1.44 and 1.27 eV for $x = 6.5$ and 16, respectively. Particularly, the slightly higher Ag/Sn molar ratio in the composition $Ba_6Ag_{2.67+4\delta}Sn_{4.33-\delta}S_{16}$ can yield solid solutions with crystal colors varying from dark-red of **1** to orange of **1a** to yellow of **1b.** The band gaps are then increased to 1.85 and 2.37 eV, respectively, relative to that of **1** (Figure 4b).

Dark-red crystals of **1** form with synthetic Ag/Sn molar ratios between 0.62 ($\delta = 0$) and 0.89 ($\delta = 0.24$). The major product of **1a** was attained at synthetic Ag/Sn molar ratios between 0.96 ($\delta = 0.30$) and 1.09 ($\delta = 0.40$), and the EDS results indicated elemental ratios distributed in a similar range of about 1.02−1.05. However, the production of larger yields of **1b**, synthetic Ag/Sn molar ratios in the range of ∼1.27 to ∼1.42, were used, which is higher than the Ag/Sn ratios characterized (in the range of 1.05−1.10). This deviation may explain why the byproducts of **1** or **1a** always formed with some **1b**. The crystal structural analyses gave the formula of **1** and **1a** with $\delta = 0.13$ and 0.30, respectively. These values correspond to ranges of δ controlled by the chemicals in the syntheses. The formula of **1b** has $\delta = 0.33$ and deviates from the synthetic Ag/Sn molar ratios applied in the reactions.

Raman Spectra. The Raman spectral pattern of **1** displays an intense peak at 336 cm^{-1} (Figure 5). The introduction of the heavier Se atoms in **3** results in a shift of the strong mode to 195 cm^{-1} and in two new weak peaks at 229 and 252 cm^{-1}. In **2**, the distribution of S and Se atoms creates fluctuations in the masses and force constants that generally lead to vibrational mode broadening.[59] The broadened Raman peaks of **2** are active at 333 cm^{-1}, 221 cm^{-1}, and 210 cm^{-1} with wavenumbers between those in **1** and **3**. The Raman spectra of **1** and **3** are similar to those of $Ag_4Sn_3Q_8$, which exhibits peaks at 314 and 178 cm^{-1} for the sulfide and selenide analogues, respectively (Supporting Information Figure S6).[60] The vibrational modes of **1** and $Ag_4Sn_3S_8$ belong to different crystal classes of $\bar{4}3m$ and 432, respectively, but the similarities in masses, force constants of the M−S (M = Ag, Sn) bonds, and local structures account for their close frequencies.

NLO Properties. The optical transparency range of the five compounds begins from their bandgap edges in the visible and ends in the infrared range at ∼20 μm (Supporting Information

Table 3. Selected Bond Distances (Å) for 1–3[a]

1		2		3	
Ba(1)–S(1)	3.153(1)	Ba(1)–S/Se(1)^{n}	3.189(1)	Ba(1)–Se(1)^{n}	3.285(1)
Ba(1)–S(1)^{b}	3.153(1)	Ba(1)–S/Se(1)^{o}	3.189(1)	Ba(1)–Se(1)^{o}	3.285(1)
Ba(1)–S(2)^{c}	3.207(1)	Ba(1)–S/Se(2)^{p}	3.265(1)	Ba(1)–Se(2)^{p}	3.313(1)
Ba(1)–S(2)^{d}	3.207(1)	Ba(1)–S/Se(2)^{q}	3.265(1)	Ba(1)–Se(2)^{q}	3.313(1)
Ba(1)–S(2)^{e}	3.314(1)	Ba(1)–S/Se(2)	3.357(1)	Ba(1)–Se(2)	3.404(1)
Ba(1)–S(2)^{f}	3.314(1)	Ba(1)–S/Se(2)^{r}	3.357(1)	Ba(1)–Se(2)^{r}	3.404(1)
Ba(1)–S(2)^{g}	3.503(1)	Ba(1)–S/Se(2)^{s}	3.546(1)	Ba(1)–Se(2)^{s}	3.620(1)
Ba(1)–S(2)^{h}	3.503(1)	Ba(1)–S/Se(2)^{t}	3.546(1)	Ba(1)–Se(2)^{t}	3.620(1)
Sn(1)–S(1)	2.359(2)	Sn(1)–S/Se(1)	2.389(2)	Sn(1)–Se(1)	2.491(2)
Sn(1)–S(2)^{i}	2.404(1)	Sn(1)–S/Se(2)^{u}	2.474(1)	Sn(1)–Se(2)^{u}	2.529(1)
Sn(1)–S(2)	2.404(1)	Sn(1)–S/Se(2)	2.474(1)	Sn(1)–Se(2)	2.529(1)
Sn(1)–S(2)^{j}	2.404(1)	Sn(1)–S/Se(2)^{q}	2.474(1)	Sn(1)–Se(2)^{q}	2.529(1)
Ag(1)–S(2)	2.586(1)	Ag(1)–S/Se(2)	2.618(1)	Ag(1)–Se(2)	2.682(1)
Ag(1)–S(2)^{h}	2.586(1)	Ag(1)–S/Se(2)^{v}	2.618(1)	Ag(1)–Se(2)^{v}	2.682(1)
Ag(1)–S(2)^{f}	2.586(1)	Ag(1)–S/Se(2)^{w}	2.618(1)	Ag(1)–Se(2)^{w}	2.682(1)
Ag(1)–S(2)^{k}	2.586(1)	Ag(1)–S/Se(2)^{s}	2.618(1)	Ag(1)–Se(2)^{s}	2.682(1)
Ag(1A)–S(2)^{k}	2.435(1)	Ag(1A)–S/Se(2)^{w}	2.470(1)	Ag(1A)–Se(2)^{w}	2.549(2)
Ag(1A)–S(2)^{f}	2.435(1)	Ag(1A)–S/Se(2)^{s}	2.470(1)	Ag(1A)–Se(2)^{s}	2.549(2)
Ag(1A)–S(2)	3.050(11)	Ag(1A)–S/Se(2)	3.067(11)	Ag(1A)–Se(2)	3.142(18)
Ag(1A)–S(2)^{h}	3.050(11)	Ag(1A)–S/Se(2)^{v}	3.067(11)	Ag(1A)–Se(2)^{v}	3.142(18)
Ag(1B)–S(2)^{k}	2.644(6)	Ag(1B)–S/Se(2)^{w}	2.717(5)	Ag(1B)–Se(2)^{w}	2.808(8)
Ag(1B)–S(2)^{f}	2.644(6)	Ag(1B)–S/Se(2)^{s}	2.717(5)	Ag(1B)–Se(2)^{s}	2.808(8)
Ag(1B)–S(1)^{l}	3.069(8)	Ag(1B)–S/Se(1)^{x}	3.077(6)	Ag(1B)–Se(2)^{x}	3.151(9)
Ag(1B)–S(1)^{m}	3.069(8)	Ag(1B)–S/Se(1)^{o}	3.077(6)	Ag(1B)–Se(2)^{o}	3.151(9)
Ag(1)···Ag(1A)	0.96(2)	Ag(1)···Ag(1A)	0.95(2)	Ag(1)···Ag(1A)	1.00(3)
Ag(1)···Ag(1B)	1.91(2)	Ag(1)···Ag(1B)	2.00(1)	Ag(1)···Ag(1B)	2.04(2)
Ag(1A)···Ag(1B)	0.95(2)	Ag(1A)···Ag(1B)	1.05(2)	Ag(1A)···Ag(1B)	1.04(3)

[a] Symmetry codes are as follows. [b] $x, -y + 1, -z + 1/2$. [c] $x - 1/4, z - 1/4, y - 1/4$. [d] $x - 1/4, -z + 5/4, -y + 3/4$. [e] $z + 1/4, y + 1/4, x - 3/4$. [f] $z + 1/4, -y + 3/4, -x + 5/4$. [g] $-x + 3/2, -y + 1, z - 1/2$. [h] $-x + 3/2, y, -z + 1$. [i] $z + 1/2, -x + 3/2, -y + 1$. [j] $-y + 3/2, -z + 1, x - 1/2$. [k] $-z + 5/4, -y + 3/4, x - 1/4$. [l] $-y + 5/4, x - 3/4, -z + 3/4$. [m] $y + 1/4, x - 3/4, z + 1/4$. [n] $-y + 1/4, -x + 3/4, z - 1/4$. [o] $y-1/4, x + 3/4, z - 1/4$. [p] $y - 1/2, z + 1/2, x + 1/2$. [q] $-y + 1/2, -z + 1, x + 1/2$. [r] $-x, -y + 3/2, z$. [s] $z - 1/4, -y + 5/4, -x + 3/4$. [t] $-z + 1/4, y + 1/4, -x + 3/4$. [u] $z - 1/2, -x + 1/2, -y + 1$. [v] $-x + 1/2, y + 0, -z + 1$. [w] $-z + 3/4, -y + 5/4, x + 1/4$. [x] $-y + 3/4, x + 3/4, -z + 5/4$.

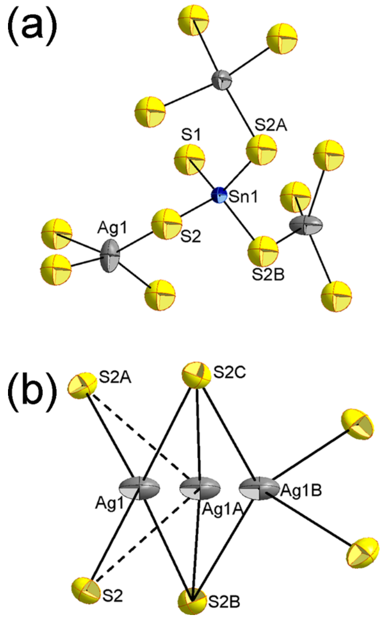

Figure 2. Thermal ellipsoid representations of (a) the partial linkage in **1** with thermal ellipsoids shown at the 60% probability level and (b) the various coordination environments of Ag(1), Ag(1A), and Ag(1B) centers at the 20% probability level.

Figure S7). We measured the SHG performance of the five samples using a tunable laser with a fundamental beam varying from 1200 to 1600 nm. The SHG intensities decreased with increasing particle size indicating that all compounds are not type-I phase matching in the spectral region examined (Figure 6).[61] The commercially used benchmarks are $AgGaS_2$ and$AgGaSe_2$ with $\chi^{(2)}$ coefficients of 36 pm/V and 66 pm/V, respectively.[62] $AgGaSe_2$ featuring the same type NLO behavior was then used as a reference.

Compound **1** with its band edge at ~785 nm (1.58 eV) absorbs some of the SHG light in the range of 600–800 nm and still exhibits strong SHG signals (Figure 7a). The absorption reduces the amount of second harmonic detected when the second harmonic lies above the bandgap. In compound **1** this was the case for all wavelengths we could access. The absorption of the sample is critical to interpreting the second harmonic generation, but it does not relate to the reliability of the data because absorption is highly reproducible. As the band edge moved to ~670 nm (1.85 eV) for compound **1a** and ~523 nm (2.37 eV) for compound **1b**, the lower interference of absorption at higher energy radiation leads to significantly enhanced SHG intensities in the range of 600–700 nm (Figure 7b,c).

The three materials **1**, **1a**, and **1b** display stronger SHG intensities relative to $AgGaSe_2$ which features a band edge at ~690 nm (1.83 eV) (Figure 8a). The orange sample of **1a** featuring the comparable bandgap to that of $AgGaSe_2$ exhibited

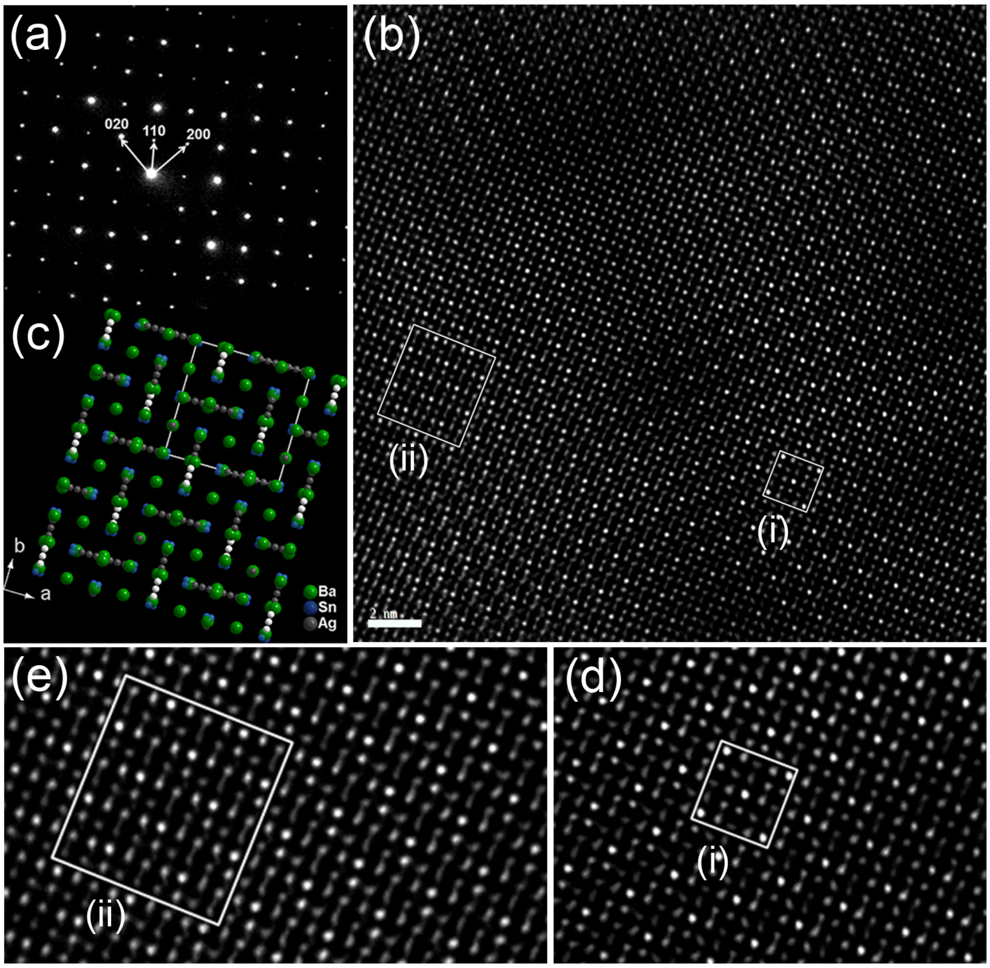

Figure 3. (a) SAED pattern from a sample of **1** along the [001] direction. (b) HREM image from a sample of **1** along the [001]. (c) The Ba(1), Sn(1), Ag(1), and Ag(1A) atoms depicted in the average structure along the [001] direction. The Ag(1B) atoms superimposed on the Ba(1) atoms with all S atoms omitted for clarity. White dots denote the arrangement of part of the silver positions corresponding to the periodic appearance of lines between barium atoms exposed in image (ii). (d) An enlarged HREM image for domain (i). (e) An enlarged HREM image for domain (ii).

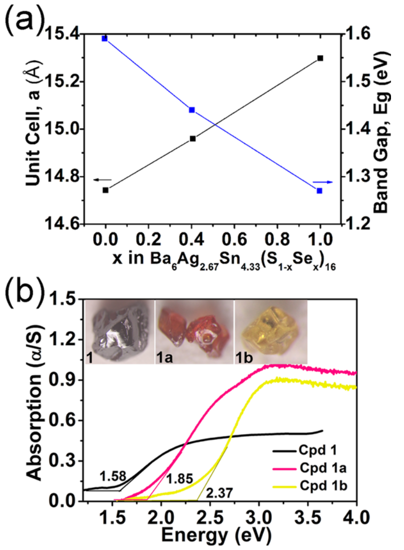

Figure 4. (a) Variation of the cubic cell dimensions of **1**, **2**, and **3** with the value of *x* in the composition $Ba_6Ag_{2.67}Sn_{4.33}(S_{1-x}Se_x)_{16}$. (b) UV−vis−NIR optical absorption spectra and typical crystal photographs of dark red **1**, orange **1a**, and yellow **1b**. Powder samples prepared from the selected crystals were used for the optical measurement.

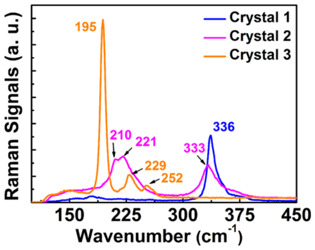

Figure 5. Raman-active phonon modes of crystals of **1**, **2**, and **3**.

SHG intensities of about 9.6, 10.6, 10.6, 11.6, and 4.4 times the reference material's SHG intensities at 600 nm, 625 nm, 650 nm, 675 nm, and 700 nm, respectively. At the longer wavelengths from 725 to 800 nm, the sample **1a** displayed the higher SHG intensities about 1.3 times. The dark-red sample of **1** with the lower band gap than that of $AgGaSe_2$ should suffer more of the extent of photon absorption. The SHG intensities of **1** at 600 nm, 625 nm, 650 nm, 675 nm, 700 nm, 725 nm, 750 nm, 775 nm, and 800 nm are still about 4.8, 6.1, 7.0, 8.8, 4.1, 1.3, 1.4, 1.6, and 1.5 times those of $AgGaSe_2$, respectively. The yellow sample of **1b** featuring the wider band gap showed more enhanced SHG intensities than the benchmark at about 7.8, 8.8, 7.9, 8.2, and 3.0 times at 600, 625, 650, 675, and 700 nm, respectively. Clearly, the

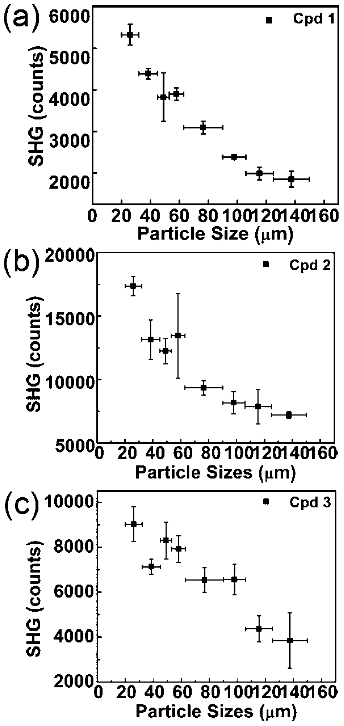

Figure 6. Particle size dependence of the SHG signal exhibiting non-type-I phase matchability for (a) **1**, (b) **2**, and (c) **3**. A 1600 nm fundamental beam was used to give the SHG responses. The errors bars are shown.

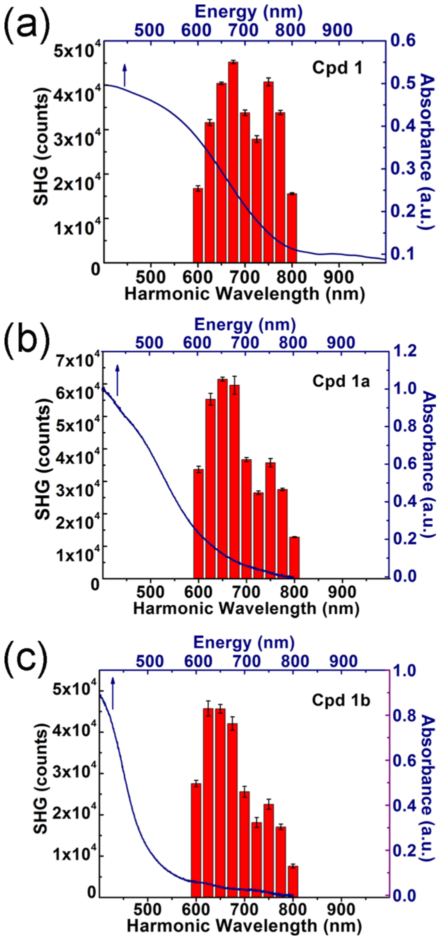

Figure 7. SHG output signal lengths between 600 and 800 nm for (a) **1**, (b) **1a**, and (c) **1b**. The optical absorption spectrum of each material is plotted (blue line) to show the limits of optical absorption of the SHG signal.

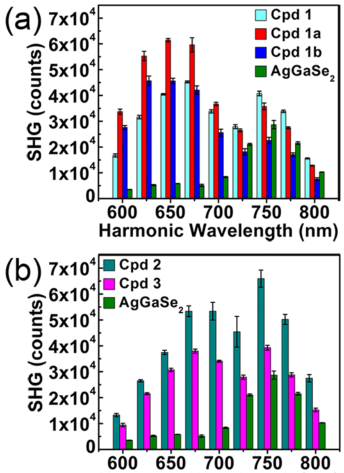

Figure 8. Comparative SHG intensities (a) for **1**, **1a**, **1b**, and reference sample of $AgGaSe_2$ and (b) for **2**, **3**, and $AgGaSe_2$.

polarizability of Ag−Q and Sn−Q bonds increases from S to Se in the series, and this enhances the SHG signals at the longer wavelengths (Figure 8b). An atomic replacement of 40% S with Se in **2** results in SHG intensities of about 10.4, 6.4, 2.2, 2.3, 2.3, and 2.7 times larger than those of $AgGaSe_2$ at 675, 700, 725, 750, 775, and 800 nm, respectively. The selenium analogue of **3** with a band edge at ~980 nm still has SHG signals superior to $AgGaSe_2$ at about 7.4, 4.1, 1.3, 1.4, 1.3, and 1.5 times the reference material's SHG intensities at 675, 700, 725, 750, 775, and 800 nm, respectively, but the severe restriction of photon absorption causes lower SHG intensities than those of **2**.

Chalcogenide compounds are particularly efficient in producing NLO materials such as Sm_4GaSbS_9,[31] $ACd_4Ga_5S_{12}$,[33] $Ba_{23}Ga_8Sb_2S_{38}$,[34] and $Ba_3CsGa_5Se_{10}Cl_2$.[35] $K_4GeP_4Se_{12}$ belonging to not type-I phase matching with SHG intensities measured in the range of 600−1200 nm outperforms $AgGaSe_2$.[47] Li_2CdGeS_4 features type-I phase matching, strong SHG signals, and high laser damage threshold in the far-IR region.[27b] The incorporation of various lanthanide metals or alkali cations in the above materials produce the SHG signals accordingly but without the shift of best performance at different wavelengths.[31,33,35,47] Uniquely, the SHG signals of the five members in this family described here are individually maximized at different wavelengths. For example, the increased degree of covalency in bonding from **1** to **2** shifts the optimal SHG response from 675 to 750 nm, respectively. Further, the solid solutions of **1**, **1a**, and **1b** with δ = 0.13, 0.31, and 0.33 characterized in the compositions $Ba_6Ag_{2.67+4\delta}Sn_{4.33-\delta}S_{16}$, respectively, display the ability to tune the bandgap energies and modify the optical properties similarly to other semiconductors such as $Al_xGa_{1-x}As$.[63]

The crystal class of the $Ba_6Ag_{2.67+4\delta}Sn_{4.33-\delta}S_{16}$ structure is $\bar{4}3m$ which is also shared by the III−V group of semiconductors. For example, in GaAs the polarized covalent bonds between Ga and As atoms in each primitive cell lead to robust NLO response.[64a] Since GaAs is a well characterized NLO crystal with a band gap of 1.43 eV, broad range of infrared transparency and a large $\chi_{xyz}^{(2)}$ coefficient about 240 pm/V, we chose to use it as a reference sample to compare with the nonlinear optical response of our $Ba_6Ag_{2.67+4\delta}Sn_{4.33-\delta}Q_{16}$ (Q = S, Se) samples.[64b]

The reflected SHG signal of the sulfide compound **1** shows clear I^2 power law dependence on the incident femtosecond laser intensity but exhibits weaker response compared to the single crystal GaAs (001) reference sample (Figure 9a). The signal ratio of I_{cpd1}(SHG)/I_{GaAs}(SHG) falls in the range of 0.03−0.11. The sulfide compound **1** features a similar resistance to laser damage as the GaAs bulk sample. It has been reported that the laser damage threshold through a 1064 nm laser is about 20 MW/cm^2 for the cubic structure of GaAs and about 10 MW/cm^2 for the chalcopyrite structure of $AgGaS_2$.[65] In contrast, the selenide compound **3** surprisingly shows 3-fold larger SHG signals than the GaAs (001) reference even with the restriction of photon absorption (Figure 9b). The signal ratio I_{cpd3}(SHG)/I_{GaAs}(SHG) falls in the range of 0.5−3.5 and is sensitive to the chosen sample spots. The SHG signal variation indicates the polycrystalline nature of the pellet samples since the SHG contribution from different single crystal facets is in fact governed by the crystal symmetry and $\chi^{(2)}$.[64a] Unfortunately, the selenide compound **3** suffers serious SHG signal reduction at higher laser intensity due to laser-induced thermal damage when the intensity is larger than 0.67 × 10^6 W/cm^2.

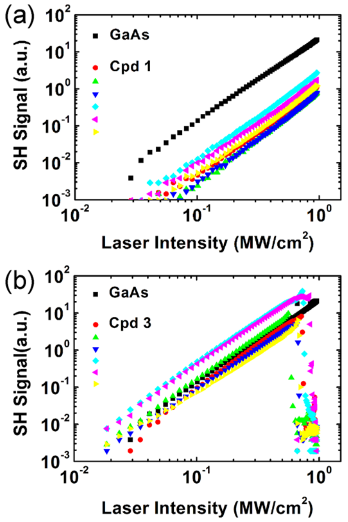

Figure 9. Laser power dependent SHG measurement for (a) sulfide compound **1** and (b) selenide compound sample **3**, where the black square symbol denotes the SHG of GaAs (100) reference sample and the other six colored symbols denote the SH signal measured in six different sample spots.

From another of point of view, the framework in **1** displays two major structural domains along the [111] direction (Figure 1b). The first domain contains the triangular-shaped infinite columns extended by the unit consisting of two Ag(1)S_4 and one Sn(1)S_4 tetrahedra. The second domain is based on the Sn(1)S_4 tetrahedra, and those connect the 3-fold related infinite columns. In both domains the orientations of Sn(1)S_4 tetrahedra mimic $GaAs_4$ tetrahedra and are arranged similarly to the zinc blende structure and have the apexes of Sn−S bonds consistently pointing upward to the (111) plane (Figure 1c). Of course we note that the crystal class of this framework, as that of GaAs, is nonpolar, where the Sn(1)S_4 tetrahedra are arranged by the $\bar{4}$ symmetry along the [100] direction and the Ag(1)S_4 tetrahedra are related by the 3-fold symmetry on the (111) plane, consistent with the nonexistence of permanent dipole moments.

The noncentrosymmetric (NCS) structures of the chalcopyrite type of $AgGaS_2$ and $ZnGeP_2$ and the zinc-blend type of GaAs belong to the nonpolar crystal classes of tetragonal $\bar{4}2m$ and cubic $\bar{4}3m$, respectively. Here we point out the geometric accumulation of dipole moments by the NSC chromophore like that the distorted tetrahedron in space does not apply to the generation of strong SHG signals (Figure 10).[65] The Sn(1)S_4 tetrahedra in **1** is deformed from an ideal T_d symmetry with the Sn(1)−S distances of 2.359(2) Å and 2.404(1) Å. The mobile Ag^+ ions in **1** certainly create a distorted tetrahedral environment. Further, the magnitude of $\chi^{(2)}$ coefficients should be related to the degree of covalency of the Ag−S and Sn−S bonds and their tendency to be polarized by the incident photons.[66,67]

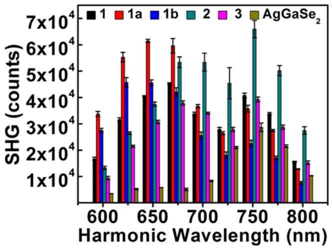

Figure 10. Comparative SHG intensities for polycrystalline samples of the five members in the series and reference $AgGaSe_2$.

■ CONCLUSIONS

The five NLO compounds based on the composition $Ba_6Ag_{2.67+4\delta}Sn_{4.33-\delta}S_{16-x}Se_x$ and the same cubic structure are of great technological importance. The disordering of silver ions in the framework does not appear to perturb the high lattice symmetry, as validated by the TEM electron diffraction studies. They represent a new family of semiconductors with the ability to control the fundamental physical properties through a range of bandgaps. Tuning of the S/Se ratio in the series generates compounds with bandgaps varying from 1.27 to 1.58 eV. Increasing the Ag/Sn molar ratio in the sulfur analogue adds two members with increased band gap up to 2.37 eV. The measured SHG signals reveal that the five members, depending on intrinsic characteristics such as covalence of the M−Q bonds and band gap energy, each have their best performance at different wavelengths (Figure 9). For example, the strongest SHG signals generated by **1b**, **1a**, **1**, **2**, and **3** occur at 625, 650, 675, 750, and 750 nm and are stronger than that of the benchmark $AgGaSe_2$ by about 8.8, 10.6, 8.8, 2.3, and 1.4 times, respectively. In addition, the resistance of **1** to laser damage is comparable to that of GaAs (001). This family of compounds includes multiple members that are suitable for further fundamental NLO investigations extending from the visible to the infrared region of the electromagnetic spectrum. The growth of single crystals required for the investigation of phase matching should be promising since all these compounds melt congruently.

■ ASSOCIATED CONTENT

Supporting Information

Crystallographic data in CIF format, PXRD patterns, and IR transmittance spectra for **1**, **1a**, **1b**, **2**. and **3**. DTA curves for **1**−**3**. TEM diffraction pattern of **1** along the $[\bar{1}13]$ direction. Raman spectra of $Ag_4Sn_3Q_8$ (Q = S, Se). UV−vis−NIR optical absorption spectra for **2** and **3**. This material is available free of charge via the Internet at http://pubs.acs.org.

■ AUTHOR INFORMATION

Notes

The authors declare no competing financial interest.

■ ACKNOWLEDGMENTS

We are grateful for the financial support of Ministry of Science and Technology (MOST) of Taiwan (NSC100-2113-M-006-004-MY2 and NSC102-2113-M-006-009). The research at Northwestern University was supported by the National Science Foundation (DMR-1410169, M.G.K., and DGE-0801685, J.B.K.) and the Institute for Sustainability and Energy at Northwestern (ISEN). A.S.H. is also supported by the National Science Foundation through a Graduate Research Fellowship under Grant No. DGE-1324585. The author Y.M.C. is grateful to acknowledge the financial support from Ministry of Science and Technology (MOST) of Taiwan under Grant No. NSC102-2119-M-002-015-MY3.

■ REFERENCES

(1) Simon, U.; Benko, Z.; Sigrist, M. W.; Curl, R. F.; Tittel, F. K. *Appl. Opt.* **1993**, *32*, 6650.

(2) Ding, Y. J. *IEEE J. Sel. Top. Quantum Electron.* **2007**, *13*, 705.

(3) Wang, L. S.; Cao, Z. S.; Wang, H. A.; Zhao, H.; Gao, W.; Yuan, Y. D.; Chen, W. D.; Zhang, W. J.; Wang, Y. J.; Gao, X. M. *Opt. Commun.* **2011**, *284*, 358.

(4) Dezaki, H.; Tanabe, T.; Oyama, Y. *J. Jpn. Inst. Met.* **2011**, *75*, 315.

(5) Smektala, F.; Quemard, C.; Leneindre, L.; Lucas, J.; Barthelemy, A.; de Angelis, C. *J. Non-Cryst. Solids* **1998**, *239*, 139.

(6) Bindra, K. S.; Bookey, H. T.; Kar, A. K.; Wherrett, B. S.; Liu, X.; Jha, A. *Appl. Phys. Lett.* **2001**, *79*, 1939.

(7) Gopinath, J. T.; Soljacic, M.; Ippen, E. P.; Fuflyigin, V. N.; King, W. A.; Shurgalin, M. *J. Appl. Phys.* **2004**, *96*, 6931.

(8) Ikuta, R.; Kusaka, Y.; Kitano, T.; Kato, H.; Yamamoto, T.; Koashi, M.; Imoto, N. *Nat. Commun.* **2011**, *2*, 537.

(9) Topfer, T.; Petrov, K. P.; Mine, Y.; Jundt, D.; Curl, R. F.; Tittel, F. K. *Appl. Opt.* **1997**, *36*, 8042.

(10) Willer, U.; Saraji, M.; Khorsandi, A.; Geiser, P.; Schade, W. *Opt. Lasers Eng.* **2006**, *44*, 699.

(11) Huff, T. B.; Shi, Y. Z.; Fu, Y.; Wang, H. F.; Cheng, J. X. *IEEE J. Sel. Top. Quantum Electron.* **2008**, *14*, 4.

(12) Adur, J.; Pelegati, V. B.; de Thomaz, A. A.; Baratti, M. O.; Almeida, D. B.; Andrade, L. A.; Bottcher-Luiz, F.; Carvalho, H. F.; Cesar, C. L. *PLoS One* **2012**, *7*, e47007.

(13) Mouras, R.; Bagnaninchi, P.; Downes, A.; Elfick, A. *J. Raman Spectrosc.* **2013**, *44*, 1373.

(14) So, P. T. C.; Yew, E. Y. S.; Rowlands, C. *Biophys. J.* **2013**, *105*, 2641.

(15) Boyd, G. D.; Kasper, H. M.; McFee, J. H. *IEEE J. Quantum Electron.* **1971**, *QE-7*, 563.

(16) Fan, Y. X.; Eckardt, R. C.; Byer, R. L. *Appl. Phys. Lett.* **1984**, *45*, 313.

(17) Canareli, P.; Benko, Z.; Curl, R. F.; Tittel, F. K. *J. Opt. Soc. Am. B* **1992**, *9*, 197.

(18) Harasaki, A.; Kato, K. *Jpn. J. Appl. Phys.* **1997**, *36*, 700.

(19) Boyd, G. D.; Kasper, H. M.; McFee, J. H.; Storz, F. G. *IEEE J. Quantum Electron.* **1972**, *QE-8*, 900.

(20) Byer, R. L.; Choy, M. M.; Herbst, R. L.; Chemla, D. S.; Feigelson, R. S. *Appl. Phys. Lett.* **1974**, *24*, 65.

(21) Simon, U.; Benko, Z.; Sigrist, M. W.; Curl, R. F.; Tittel, F. K. *Appl. Opt.* **1993**, *32*, 6650.

(22) Petrov, V.; Badikov, V.; Shevyrdyaeva, G.; Panyutin, V.; Chizhikov, V. *Opt. Mater.* **2004**, *26*, 217.

(23) Petrov, V.; Noack, F.; Badikov, V.; Shevyrdyaeva, G.; Panyutin, V.; Chizhikov, V. *Appl. Opt.* **2004**, *43*, 4590.

(24) Tyazhev, A.; Marchev, G.; Vedenyapin, V.; Kolker, D.; Yelisseyev, A.; Lobanov, S.; Isaenko, L.; Zondy, J. J.; Petrov, V. *Proc. SPIE* **2010**, *7582*, 75820E.

(25) Tyazhev, A.; Vedenyapin, V.; Marchev, G.; Isaenko, L.; Kolker, D.; Lobanov, S.; Petrov, V.; Yelisseyev, A.; Starikova, M.; Zondy, J. J. *Opt. Mater.* **2013**, *35*, 1612.

(26) Kim, Y.; Seo, I.; Martin, S. W.; Baek, J.; Halasyamani, P. S.; Armugam, N.; Steinfink, H. *Chem. Mater.* **2008**, *20*, 6048.

(27) (a) Lekse, J. W.; Moreau, M. A.; McNerny, K. L.; Yeon, J.; Halasyamani, P. S.; Aitken, J. A. *Inorg. Chem.* **2009**, *48*, 7516. (b) Brant, J. A.; Clark, D. J.; Kim, Y. S.; Jang, J. I.; Zhang, J. H. *Chem. Mater.* **2014**, *26*, 3045.

(28) Chung, I.; Kanatzidis, M. G. *Chem. Mater.* **2014**, *26*, 849.

(29) Lin, X.; Zhang, G.; Ye, N. *Cryst. Growth. Des.* **2009**, *9*, 1186.

(30) Yao, J.; Mei, D.; Bai, L.; Lin, Z.; Yin, W.; Fu, P.; Wu, Y. *Inorg. Chem.* **2010**, *49*, 9212.

(31) Chen, M. C.; Li, L. H.; Chen, Y. B.; Chen, L. *J. Am. Chem. Soc.* **2011**, *133*, 4617.

(32) Yin, W.; Feng, K.; Mei, D.; Yao, J.; Fu, P.; Wu, Y. *Dalton Trans.* **2012**, *41*, 2272.

(33) (a) Lin, H.; Zhou, L. J.; Chen, L. *Chem. Mater.* **2012**, *24*, 3406. (b) Lin, H.; Chen, L.; Zhou, L. J.; Wu, L. M. *J. Am. Chem. Soc.* **2013**, *135*, 12914.

(34) Chen, M. C.; Wu, L. M.; Lin, H.; Zhou, L. J.; Chen, L. *J. Am. Chem. Soc.* **2012**, *134*, 6058.

(35) Yu, P.; Zhou, L. J.; Chen, L. *J. Am. Chem. Soc.* **2012**, *134*, 2227.

(36) Kuo, S. M.; Chang, Y. M.; Chung, In; Jang, J. I.; Her, B. H.; Yang, S. H.; Ketterson, J. B.; Kanatzidis, M. G.; Hsu, K. F. *Chem. Mater.* **2013**, *25*, 2427.

(37) Zhang, M. J.; Li, B. X.; Liu, B. W.; Fang, Y. H.; Li, X. G.; Zheng, H. Y.; Guo, G. C. *Dalton Trans.* **2013**, *42*, 14223.

(38) Liao, J. H.; Marking, G. M.; Hsu, K. F.; Matsushita, Y.; Ewbank, M. D.; Borwick, R.; Cunningham, P.; Rosker, M. J.; Kanatzidis, M. G. *J. Am. Chem. Soc.* **2003**, *125*, 9484.

(39) Chung, I.; Song, J. H.; Jang, J. I.; Freeman, A. J.; Kanatzidis, M. G. *J. Solid State Chem.* **2012**, *195*, 161.

(40) Lin, X.; Guo, Y.; Ye, N. *J. Solid State Chem.* **2012**, *195*, 172.

(41) Yin, W.; Feng, K.; Hao, W.; Yao, J.; Wu, Y. *Inorg. Chem.* **2012**, *51*, 5839.

(42) Luo, Z. Z.; Lin, C. S.; Cheng, W. D.; Zhang, H.; Zhang, W. L.; He, Z. Z. *Inorg. Chem.* **2013**, *52*, 273.

(43) Chen, M. C.; Li, P.; Zhou, L. J.; Li, L. H.; Chen, L. *Inorg. Chem.* **2013**, *50*, 12402.

(44) Chung, I.; Malliakas, C. D.; Jang, J. I.; Canlas, C. G.; Weliky, D. P.; Kanatzidis, M. G. *J. Am. Chem. Soc.* **2007**, *129*, 14996.

(45) Chung, I.; Song, J. H.; Jang, J. I.; Freeman, A. J.; Ketterson, J. B.; Kanatzidis, M. G. *J. Am. Chem. Soc.* **2009**, *131*, 2647.

(46) Chung, I.; Jang, J. I.; Malliakas, C. D.; Ketterson, J. B.; Kanatzidis, M. G. *J. Am. Chem. Soc.* **2010**, *132*, 384.

(47) Morris, C. D.; Chung, I.; Park, S.; Harrison, C. M.; Clark, D. J.; Jang, J. I.; Kanatzidis, M. G. *J. Am. Chem. Soc.* **2012**, *134*, 20733.

(48) *APEX*, version 2008.2-0; Bruker Analytical X-ray Systems: Madison, WI, 2006.

(49) Sheldrick, G. M. *SHELXTL-Plus NT crystallographic system*, version 6.1; Bruker Analytical X-ray Systems: Madison, WI, 2000.

(50) Spek, A. L. *Acta Crystallogr.* **1990**, *A46*, C34.

(51) Tandon, S. P.; Gupta, J. P. *Phys. Status Solidi* **1970**, *38*, 363.

(52) McCarthy, T. J.; Ngeyi, S. P.; Liao, J. H.; Degroot, D. C.; Hogan, T.; Kannewurf, C. R.; Kanatzidis, M. G. *Chem. Mater.* **1993**, *5*, 331.

(53) Johnsen, S.; Peter, S. C.; Nguyen, S. L.; Song, J. H.; Jin, H.; Freeman, A. J.; Kanatzidis, M. G. *Chem. Mater.* **2011**, *23*, 4375.

(54) Teske, C. L. *Z. Anorg. Allg. Chem.* **1985**, *522*, 122.
(55) Burdett, J. K.; Eisenstein, O. *Inorg. Chem.* **1992**, *31*, 1758.
(56) Daszkiewicz, M.; Gulay, L. D.; Lychmanyuk, O. S. *Acta Crystallogr.* **2009**, *B65*, 126.
(57) Williams, D. B.; Carter, C. B. *Transmission Electron Microscopy: A Textbook for Material Science*, 2nd ed.; Springer: New York, 2009.
(58) Denton, A. R.; Ashcroft, N. W. *Phys. Rev. A* **1991**, *43*, 3161.
(59) Guler, I.; Gasanly, N. M. *Physica B* **2011**, *406*, 3374.
(60) Hull, S.; Berastegui, P.; Grippa, A. *J. Phys.: Condens. Matter* **2005**, *17*, 1067.
(61) Kurtz, S. K.; Perry, T. T. *J. Appl. Phys.* **1968**, *39*, 3798.
(62) Bhar, G. C. *Jpn. J. Appl. Phys., Part 1* **1993**, *32*, 653.
(63) Alferov, Z. I. *Semiconductors* **1998**, *32*, 1.
(64) (a) Boyd, R. W. *Nonlinear Opt.*; Academic Press: New York, 1992. (b) Bergfeld, S.; Daum, W. *Phys. Rev. Lett.* **2003**, *90*, 036801-1.
(65) Romann, A.; Sigrist, M. W. *Proc. SPIE* **2002**, *4618*, 1605.
(66) (a) Halasyamani, P. S.; Poeppelmeier, K. R. *Chem. Mater.* **1998**, *10*, 2753. (b) Chen, C.; Sasaki, T.; et al. *Nonlinear Optical Borate Crystals: Principles and Applications*; Wiley-VCH, 2012.
(67) (a) Zhao, S.; Jiang, X.; He, R.; Zhang, S.; Sun, Z.; Luo, J.; Lin, Z.; Hong, M. *J. Mater. Chem. C* **2013**, *1*, 2906. (b) Jian, X.; Zhao, S.; Lin, Z.; Luo, J.; Bristowe, P. D.; Guan, X.; Chen, C. *J. Mater. Chem. C* **2014**, *2*, 530.

DOI: 10.1021/cm504348z